

Radiance Field Delta Video Compression in Edge-Enabled Vehicular Metaverse

Matúš Dopiriak¹, Eugen Šlapak¹, Juraj Gazda¹, Devendra S. Gurjar²,
Mohammad Abdullah Al Faruque³, Marco Levorato³

¹Department of Computers and Informatics, Technical University of Košice, Slovakia
Email: {matus.dopiriak, eugen.slapak, juraj.gazda}@tuke.sk

²Department of Electronics and Communications Engineering, National Institute of Technology Silchar, Assam, India
Email: dsgurjar@ece.nits.ac.in

³Department of Electrical Engineering and Computer Science, University of California, Irvine, United States
Email: {alfaruqu, levorato}@uci.edu

Abstract—Connected and autonomous vehicles (CAVs) offload computationally intensive tasks to multi-access edge computing (MEC) servers via vehicle-to-infrastructure (V2I) communication, enabling applications within the vehicular metaverse, which transforms physical environment into the digital space enabling advanced analysis or predictive modeling. A core challenge is physical-to-virtual (P2V) synchronization through digital twins (DTs), reliant on MEC networks and ultra-reliable low-latency communication (URLLC). To address this, we introduce radiance field (RF) delta video compression (RFDVC), which uses RF-encoder and RF-decoder architecture using distributed RFs as DTs storing photorealistic 3D urban scene in compressed form. This method extracts differences between CAV-frame capturing actual traffic and RF-frame capturing empty scene from the same pose in batches encoded and transmitted over the MEC network. Experiments show data savings up to 90% against H.264 codec and 45% against H.265 codec under different conditions as lighting changes, rain and fog. RFDVC exhibits greater resilience to transmission errors, achieving a bit error rate (BER) of approximately $10^{-1.6}$ at signal-to-noise ratio (SNR) of 10 dB, compared to $10^{-1.4}$ for standard video coding.

Index Terms—autonomous driving, digital twin, edge computing, radiance fields, vehicular metaverse, video compression.

I. INTRODUCTION

CONNECTED and autonomous vehicles (CAVs) are at the forefront of modern transportation systems, relying on advanced perception module to process terabytes of data from sensors, e.g., LiDARs or cameras. The module interprets the environment to ensure safe and efficient navigation by executing computationally intensive tasks such as localization, object detection, scene understanding, prediction, and tracking in real-time [1]. To manage these high demands, CAVs employ vehicle-to-infrastructure (V2I) communication, offloading processing tasks to edge computing servers [2].

Tech giants have recently invested heavily towards transforming physical environment into the digital space within the metaverse [3], including applications in transportation systems, known as vehicular metaverse. It integrates real-time traffic information into a unified virtual space, enabling advanced analysis, predictive modeling, and efficient resource management. A key challenge in this domain is the physical-to-virtual (P2V) synchronization [4], which relies on V2I

communication utilizing multi-access edge computing (MEC) networks [5] and ultra-reliable low latency communications (URLLC) [6] requiring reliability levels up to $1 - 10^{-5}\%$ and end-to-end latency in the range of 5 – 10 ms. In recent years, deep learning (DL) techniques have been employed to enhance P2V synchronization and meet stringent communication requirements through video compression [7], [8]. These techniques are primarily used in conjunction with standard video codecs for intra-prediction, focusing on compressing intra frames (complete frames), which contribute the most to the overall bitrate. Additionally, other approaches use implicit neural representations to transform individual frames [9]–[11] or use learning-based compression of both temporal and binocular redundancy in stereo video [12].

The metaverse endeavors to close this synchronization gap by developing photorealistic digital environments, i.e, digital twins (DTs) at the edge of the MEC network [13]–[15]. Recent studies as in [16]–[20] also underscore the critical role of DTs at the edge in reconstructing alternative digital environments that do not require advanced sensor data, such as LiDARs, nor their redundant transmission over the network.

Since 2020, neural radiance fields (NeRFs) [21] have become a significant breakthrough in a 3D scene reconstruction and rendering, enabling potential DT applications without relying on LiDAR data transmission over the MEC network. This is achieved through implicit depth prediction via volume rendering along a ray and the development of advanced NeRF variants. NeRFs enable the generation of novel views from previously unseen angles and provide efficient compression of 3D scenes, even when trained on sparse input data with varying camera poses. The underlying volumetric representation is encoded as a multi-layer perceptron (MLP) and rendered through volumetric ray-marching. NeRFs excel in modeling volumetric radiance, which is crucial for accurately capturing intricate details, subtle lighting effects, and complex lighting conditions, such as advanced reflections and dynamic weather changes, essential for a realistic scene reconstruction. In recent years, significant advancements have been made in reducing training and rendering time while improving the accuracy of radiance fields (RFs) as in [22], [23], especially instant neural

graphics primitives (INGP) [24] and 3D gaussian splatting (3DGS) [25] explained more in-depth in subsection II-B.

In the survey on the application of RFs in autonomous driving (AD) [26], traditional RF methods are highlighted as struggling with scalability, leading to visual artifacts and reduced fidelity in large outdoor environments. To address this issue, Block-NeRF [27] was proposed, decomposing extensive scenes into multiple compact, independently trained NeRFs. While recent advancements offer promising solutions to large-scale scenes, they are hindered by significant computational demands. Streamable memory efficient RF (SMERF) [28] introduces a hierarchical model partitioning scheme and distillation training, while NeRF-XL [29] distributes tasks across multiple GPUs. Hierarchical 3DGS [30] partitions large scenes into chunks, optimizing each independently.

RF-based simulators [31]–[33] are utilizing scene decomposition of dynamic elements and scene relighting to be primarily used for further simulations in AD or secondarily be used as DTs. However, the experimental results lack robustness for generalization across diverse scenarios and depend on LiDAR data for computationally intensive training. Distributed visual data collection for creation of NeRF-based DT for autonomous mobility was examined in [34]. The work has tested the speed of real-world to DT updates when considering different DT quality and network conditions. While this work tests many of the assumptions crucial for our work, it misses the key idea of use of NeRFs for rapid compression to mitigate the latency.

In this study, we extend our previous work in [35] by introducing RF delta video compression (RFDVC). This approach leverages a hybrid communication between a CAV and a MEC server. RFs, distributed across the CAV (sender) and the MEC server (receiver), reconstruct static elements of an empty urban scene such as buildings and traffic lights, reducing the need for their repeated transmission. We segment differences between CAV-frame and RF-frame such as vehicles and pedestrians represented as delta-frames. The sender encodes and transmits delta-frames in batches, while the receiver reconstructs the CAV-frame by applying the delta-frame to the corresponding RF-frame generated from the same camera pose. Standard codecs face challenges encoding complex patterns within or across frames, leading to increased bitrate and potential MEC network congestion. RFDVC minimizes redundant data by storing it in distributed RFs at both ends, while delta-frames retain only differences between CAV-frame and RF-frame. Remaining pixels are masked out as a solid black background enabling more efficient compression. RFDVC achieves notable throughput savings and reduces latency pivotal for a real-time communication.

The main contributions of this paper are summarized as follows:

- 1) We present a RF-based encoder-decoder architecture that leverages distributed RFs as DTs for efficient and compressed 3D representation of urban scenes in the vehicular metaverse.
- 2) We propose delta segmentation (DS) algorithm for extraction of differences between CAV-frame and RF-

frame pairs without being limited by predefined set of classes.

- 3) We validate the data savings of the RFDVC framework compared to H.264 and H.265 codecs across various environment conditions, i.e., lighting, wet, rain and fog. We evaluate its performance under simulated packet loss to assess quality under challenging network conditions.

II. VIDEO COMPRESSION PRELIMINARIES

We present the foundational principles of the H.264 and H.265 codecs widely utilized for real-time video streaming to achieve efficient video compression via inter-frame and intra-frame encoding techniques. Subsequently, we introduce RFs as compressed representations of 3D scenes.

A. Standard Video Compression

Standard video codecs like H.264 and H.265 (HEVC) are critical for real-time video streaming, including applications in V2I communication. These codecs use spatial compression to eliminate redundancy within individual frames and temporal compression to minimize redundancy across multiple frames. Frames are generally organized into a group of pictures (GOP) structure, defined as the interval between two complete frames, known as intra-frames. The GOP consists of both intra-frames (I-frames) and inter-frames. I-frames store the full image information, similar to a standard jpeg file. Inter-frames, which depend on I-frames for reconstruction, are categorized into P-frames and B-frames. P-frames store differences from preceding frames, while B-frames store differences from both preceding and subsequent frames. B-frames achieve the highest compression and have the smallest file size among these frame types. Fig. 2 b) shows a sequence of encoded frames transmitted over the network within a GOP structure. It highlights the arrangement of B-frames and P-frames between two I-frames.

Traditional video compression depends on frequent I-frame transmission to maintain video quality, especially in scenes with high motion or complexity, as P-frames and B-frames rely on I-frames for reconstruction. Extending the GOP length can reduce the overall data size by decreasing the number of I-frames, which are the largest contributors to the GOP size. However, this approach may reduce frame reconstruction quality and increase vulnerability to errors caused by network issues, such as packet loss or bit flips. To balance compression efficiency, video quality, and latency, careful management of I-frame transmission frequency, or even avoiding frequent I-frame transmission, is necessary to prevent network congestion. In the context of CAVs, maintaining low latency remains a crucial challenge, and the compression of I-frames is still a significant bottleneck in standard video coding (VC) when deployed for real-time data transmission.

B. Radiance Fields as Compressed 3D Scenes

We explore the core principles of RFs pivotal to our approach for efficient and photorealistic compression of 3D scenes used as DTs in the vehicular metaverse. We focus on

two RF variants used in our experiments: INGP [24] and 3DGS [25]. These variants were selected primarily for their strong contributions in favorable training time and the reasonable accuracy they offer in reconstructing 3D scenes.

NeRFs [21] utilize MLPs to encode 3D scenes, parametrizing images with camera poses and optimizing a volumetric scene function approximated by MLP P_{Θ} :

$$P_{\Theta} : (\mathbf{x}, \mathbf{d}) \rightarrow (\hat{c}, \sigma), \quad (1)$$

where \mathbf{x} is the location of the point in 3D space, \mathbf{d} is the viewing direction, \hat{c} is the emitted radiance, and σ is the volume density.

Rendering from RF involves calculating the expected color $\hat{C}(\mathbf{r})$ of a ray $\mathbf{r}(t) = \mathbf{o} + t\mathbf{d}$, defined by its origin \mathbf{o} and direction \mathbf{d} , within near and far bounds t_n and t_f , by integrating transmittance $T(t)$:

$$\hat{C}(\mathbf{r}) = \int_{t_n}^{t_f} T(t)\sigma(\mathbf{r}(t))\hat{c}(\mathbf{r}(t), \mathbf{d})dt. \quad (2)$$

The transmittance $T(t)$ is defined as follows:

$$T(t) = \exp\left(-\int_{t_n}^t \sigma(\mathbf{r}(s))ds\right), \quad (3)$$

where $T(t)$ is the probability that ray in the range from t_n to t does not hit any material.

The loss \mathcal{L}_{NeRF} is the squared error between rendered $\hat{C}(\mathbf{r})$ and ground truth (GT) $C(\mathbf{r})$ colors:

$$\mathcal{L}_{NeRF} = \sum_{\mathbf{r} \in \mathcal{R}} [\|\hat{C}(\mathbf{r}) - C(\mathbf{r})\|_2^2], \quad (4)$$

where \mathcal{R} is the set of rays in each batch.

We describe our INGP and 3DGS, which use images captured from different angles and camera pose information as a transformation matrix. This data is typically obtained through a structure from motion (SfM) algorithm from CAV-frames or by transforming camera poses from the CARLA simulator to the Nerfstudio library, as shown in our experiments using the following formula:

$$M_{ns} = R_z(90) \cdot R_x(-90) \cdot R_y(180) \cdot T \cdot M_{cl}, \quad (5)$$

where M_{ns} is a transformation matrix of the Nerfstudio library, R_z, R_x, R_y represent rotation matrices for each axis, T is a transformation matrix substituting each axis and M_{cl} is a transformation matrix of the CARLA simulator.

INGP [24] tackles the issue of NeRFs in excessive training and rendering times using neural graphics primitives and multiresolution hash encoding. The model contains trainable weight parameters ϕ and encoding parameters θ structured into L levels, each holding up to U feature vectors. Each level $l \in L$ operates independently, storing feature vectors at grid vertices. The grid resolution at each level l follows a geometric progression from the coarsest N_{min} to the finest N_{max} resolution given by formulas:

$$N_l := N_{min} \cdot b^l, \quad (6)$$

where N_l is the resolution at level l , and b is the growth factor:

$$b := \exp\left(\frac{\ln N_{max} - \ln N_{min}}{L - 1}\right). \quad (7)$$

The 3DGS [25] uses differentiable 3D gaussians to model scenes without the use of neural components. 3DGS constructs 3D gaussians $G(x)$ in world space centered at point (mean) μ , and represented by covariance matrix Σ :

$$G(x) = \exp\left(-\frac{1}{2}(x)^T \Sigma^{-1}(x)\right). \quad (8)$$

These gaussians are projected to 2D using a transformation W and jacobian J , resulting in a camera-space covariance matrix Σ' :

$$\Sigma' = JW\Sigma W^T J^T. \quad (9)$$

The covariance matrix Σ defines scaling S and rotation R :

$$\Sigma = RSS^T R^T. \quad (10)$$

Stochastic gradient descent (SGD) optimizes gaussian parameters p, α, Σ , and spherical harmonics (SH) representing color c of each gaussian. The loss function \mathcal{L}_{3DGS} combines mean absolute error \mathcal{L}_1 and a differentiable structural similarity index measure (SSIM) \mathcal{L}_{D-SSIM} with a balance hyperparameter λ :

$$\mathcal{L}_{3DGS} = (1 - \lambda)\mathcal{L}_1 + \lambda\mathcal{L}_{D-SSIM}. \quad (11)$$

III. FORMULATION OF THE PROBLEM

In this section, we present the V2I communication problem, introducing all mathematical notations used for both the problem formulation and the proposed approach, as summarized in Table I.

V2I communication is implemented within the city map \mathcal{M} . Given the limitations of RFs to smaller scenes, we segment the city's road network into distinct areas $a \in \mathcal{M}$, as depicted in Fig. 1. The map is color-coded, with highways represented in red and intersections in green. In total, the map consists of 19 areas, each designed to correspond to specific regions of interest within the simulation environment.

The V2I communication employs \mathcal{V} as the set of CAVs and \mathcal{E} as the set of MEC servers. Each CAV $v \in \mathcal{V}$ transmits batch of video frames, i.e., CAV-frames F_{cav} , to its assigned MEC server $e \in \mathcal{E}$. Frames are grouped into batches of a specified size, denoted by \mathbf{B}_{cav} , and encoded before transmission. Transmitted bitstream \mathbf{b}_{stream} is decoded on the receiver side for downstream tasks.

Fig. 2 illustrates a CAV v (sender) offloading batch of CAV-frames \mathbf{B}_{cav} over the MEC network to a nearby MEC server e (receiver). A primary challenge arises from the typical use of codecs like H.264, which encode frame batches with reference and complete frames, resulting in larger data sizes and potential network congestion. Our objective is to reduce network communication overhead while ensuring that the transmitted frame batches preserve the semantic information required for subsequent downstream tasks on MEC servers.

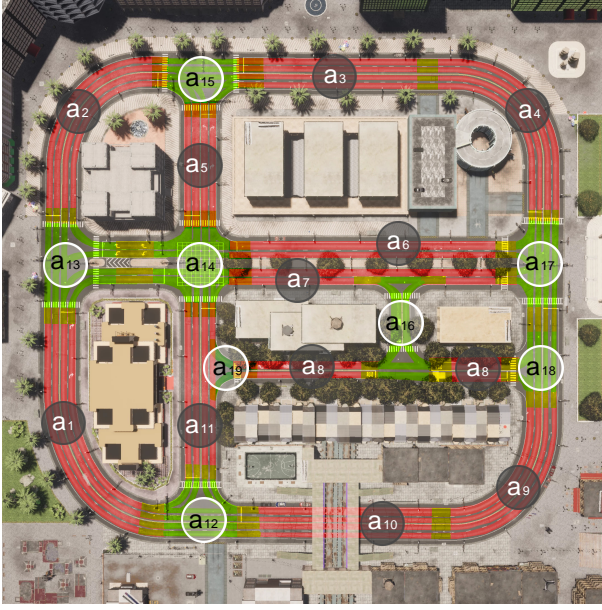


Fig. 1. CARLA map divided into 19 areas, each represented as RF model. Highways are depicted in red and intersections in green.

TABLE I
MAIN NOTATIONS

Notation	Description
\mathcal{M}	Map
a	Area within a map
\mathcal{V}	The set of CAVs
v	CAV
\mathcal{E}	The set of MEC servers
e	MEC server
\mathbf{b}_{stream}	Bitstream
\mathbf{B}_{Δ}	The batch of delta-frames
\mathbf{B}_{cav}	The batch of CAV-frames
\mathbf{B}_{rec}	The batch of rec-frames
Ψ_{rf}	RF model
π	Camera pose
F_{cav}	CAV-frame
F_{rf}	RF-frame
F_{Δ}	Delta-frame
F_{rec}	Rec-frame
S_{cav}	Seg-frame from CAV-frame
S_{rf}	Seg-frame from RF-frame
S_{Δ}	Seg-frame with differences
Δ	Encoded delta
Δ_{tx}	Transmitted Δ
Th	Throughput
τ	Estimated transmission time

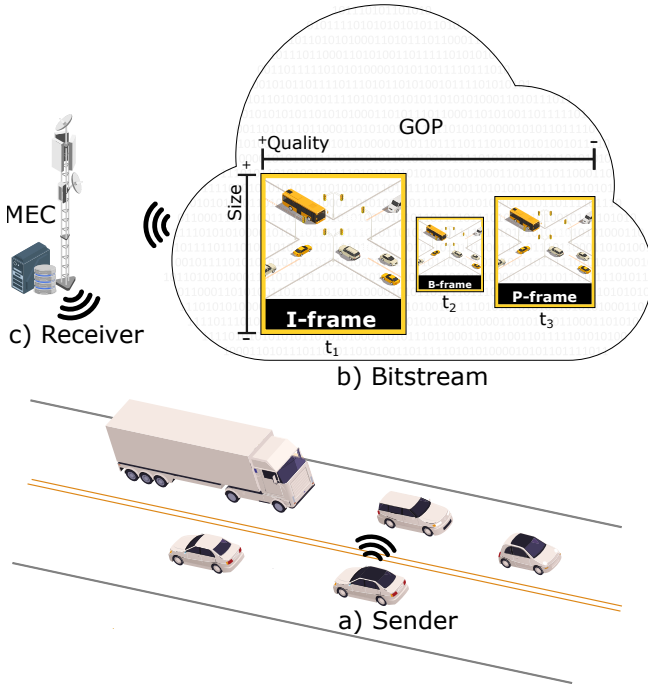


Fig. 2. V2I communication between a CAV and a MEC server. (a) Sender v captures CAV-frames using onboard cameras. (b) A batch of CAV-frames \mathbf{B}_{cav} is transmitted over the network as a bitstream \mathbf{b}_{stream} . (c) Receiver e processes the data and returns the output to the sender.

IV. PROPOSED RADIANCE FIELD DELTA VIDEO COMPRESSION

Efficient video streaming is critical in CAVs for transmitting high-resolution frames from onboard cameras to MEC servers for subsequent processing. In this section, we propose RFDVC, a method aimed at minimizing latency and optimiz-

ing network performance by transmitting only novel or critical data, thereby excluding redundant and repetitive information.

A. Formulation of RFDVC Problem

The proposed method employs an encoder-decoder architecture optimized for V2I communication between CAV and a MEC server, leveraging RFs distributed on both ends. On the CAV side (sender), we use a RF-encoder as depicted in Fig. 3 a) The CAV is equipped with multiple onboard cameras that continuously capture the surrounding environment in real-time as CAV-frames. Concurrently, a pretrained RF model generates RF-frames from the same camera poses, which represent an empty environment devoid of dynamic objects, such as vehicles. For each camera pose, we obtain a pair of frames: a CAV-frame reflecting the current traffic conditions and a RF-frame representing the static environment.

Our objective is to minimize the amount of data transmitted over the network. To achieve this, we extract differences between image pairs to generate delta-frames. We employ a DS algorithm to process the CAV-frame and RF-frame pairs, producing delta-frames that are encoded using a standard video codecs. The distributed RF model serves as the I-frame (a complete frame), thus I-frame does not have to be transmitted, allowing only novel data along with the corresponding camera poses to be transmitted to the MEC server.

Fig. 3 b) illustrates the RF-decoder on the MEC server side (receiver). Using the received camera poses, RF-frames are generated with the same RF model employed at the server side. Upon receiving the encoded delta-frames, the server decodes them and merges these delta-frames with the corresponding RF-frames to reconstruct the original CAV-frames, called rec-frames. Advanced DL techniques are then applied to the rec-frames to perform downstream tasks such as object detection, semantic segmentation or advanced scene understanding.

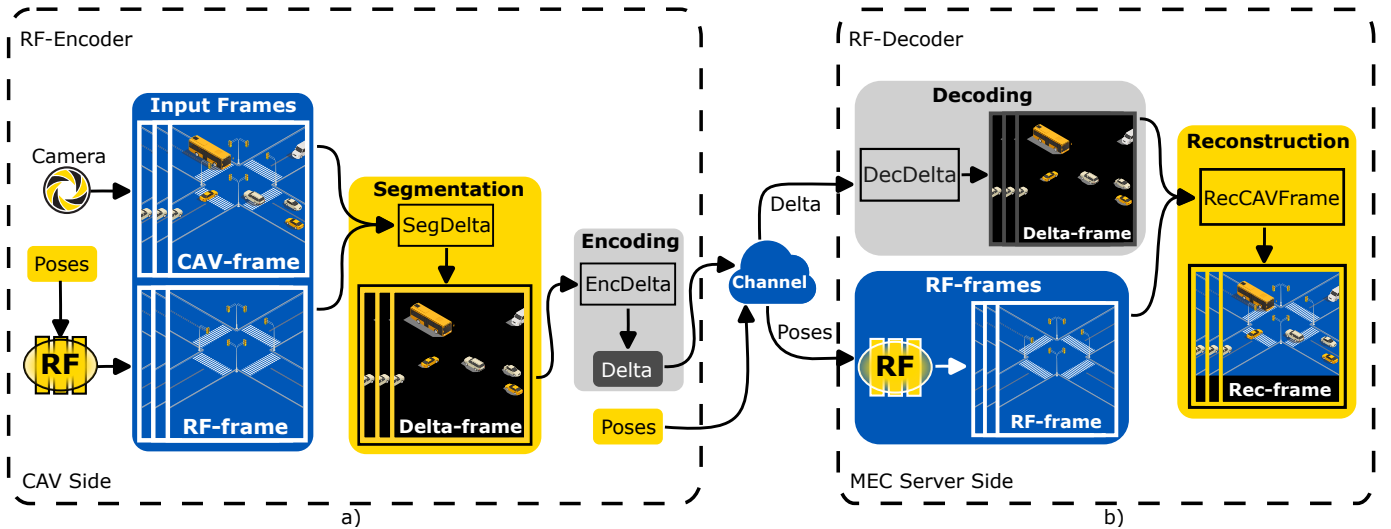


Fig. 3. The proposed RFDVC utilizes distributed RFs within the MEC network. The diagram shows a) (a) RF-encoder extracts pairs of input CAV-frames and RF-frames to segment delta-frames using the DS algorithm. Delta-frames are then encoded via the H.264/H.265 codec and transmitted over the channel. (b) The RF-decoder subsequently decodes the delta and combines delta-frames with RF-frames to reconstruct rec-frames.

Alg. 1 comprises three core procedures `RFEncoder`, `ChannelTX`, and `RFDecoder` designed to optimize frame encoding, network transmission, and decoding using RFs. In the `RFEncoder` procedure, lines 1-11 iterate over each frame in `CAV_Frames`, where the camera pose is extracted, RF-frame is rendered based on the pose, and the delta-frame is computed by comparing CAV-frame and RF-frame. These computed delta-frames are accumulated in a list and subsequently encoded. The `ChannelTX` procedure, detailed in lines 12-19, segments the encoded deltas for transmission according to the available network throughput, ensuring that data is sent efficiently with minimal delay. During transmission, any lost packets are replaced with black pixels to maintain the frame structure and mitigate data loss. Finally, the `RFDecoder` procedure, represented by lines 20-31, receives the transmitted deltas, decodes them, and reconstructs each frame by merging the decoded delta-frame with a freshly rendered RF-frame aligned to the transmitted pose, preserving frame integrity upon reception. This three stage process reduces bandwidth by transmitting only delta information, thereby enabling efficient, high-quality frame reconstruction on the receiver side.

B. Delta Segmentation

We obtain images from both the trained RF model as RF-frames and the camera of a CAV as CAV-frames, resulting in a pair of differing images. By transforming both images into a simplified form, we facilitate the segmentation of all possible dissimilarities between them without being limited by class categories as using you only look once (YOLO) for classification tasks or Mask-RCNN for segmentation tasks.

We employ the segment anything model (SAM) [36] because it demonstrates strong zero-shot generalization and superior performance across various segmentation tasks, including

semantic segmentation. SAM is capable of performing effectively on tasks for which it was not explicitly trained, thereby showcasing its robustness and versatility in segmenting objects beyond limited class categories. While SAM aims to create a highly accurate foundational segmentation model based on transformer architecture, it demands substantial computational power, making it unsuitable for real-time applications. In contrast, FastSAM [37], an accelerated variant using convolutional neural networks (CNNs), is 50 times faster than SAM while achieving comparable accuracy. Consequently, FastSAM can be effectively deployed in CAVs for real-time segmentation tasks.

We compare F_{cav} and F_{rf} with potential differences. Applying FastSAM to both frames, we obtain two seg-frames \mathcal{S}_{cav} and \mathcal{S}_{rf} . The comparison between the masks is performed using the intersection over union (IoU) metric:

$$\text{IoU}(\mathcal{S}_{cav}, \mathcal{S}_{rf}) = \frac{|\mathcal{S}_{cav} \cap \mathcal{S}_{rf}|}{|\mathcal{S}_{cav} \cup \mathcal{S}_{rf}|}, \quad (12)$$

where $|\cdot|$ denotes the area of the masks.

A match between masks is identified when the IoU exceeds a predefined threshold. Masks without a match, i.e., IoU below the threshold, are considered as differences. All these masks are stored in the seg-frame \mathcal{S}_{Δ} .

The simulation environment facilitates the extraction of both RGB images and GT segmentation masks, which are then processed to retain only vehicles and pedestrians, with the remaining areas of the image represented by black pixels. It is assumed that the RF models used in this process exhibit no discrepancies and that the environment contains no additional objects. Fig. 4 depicts both the delta-frames extracted from the GT masks and proposed DS algorithm in sparse and dense traffic. DS method allows for the extraction of all relevant information necessary for downstream tasks without requiring knowledge of the exact object class. However, distant objects

Algorithm 1 RF-Encoder, Network Transmission, and RF-Decoder

```

1: procedure RFENCODER( $\mathbf{B}_{cav}, \Psi_{rf}$ )
2:    $\mathbf{B}_{\Delta} \leftarrow$  empty list
3:   for  $F_{cav} \in \mathbf{B}_{cav}$  do
4:      $\pi \leftarrow$  ExtractPose( $F_{cav}$ )
5:      $F_{rf} \leftarrow$  RenderViewFromRF( $\Psi_{rf}, \pi$ )
6:      $F_{\Delta} \leftarrow$  SegDelta( $F_{cav}, F_{rf}$ )
7:     Add( $\mathbf{B}_{\Delta}, (\pi, F_{\Delta})$ )
8:   end for
9:    $\Delta \leftarrow$  EncDelta( $\mathbf{B}_{\Delta}$ )
10:  return  $\Delta$ 
11: end procedure

12: procedure CHANNELTX( $\Delta, Th$ )
13:   $\Delta_{tx} \leftarrow$  empty list
14:   $|\Delta| \leftarrow$  GetSize( $\Delta$ )
15:   $\tau \leftarrow |\Delta|/Th$ 
16:  TransmitOverChannel( $\Delta, \tau$ )
17:  Add( $\Delta_{tx}, (\Delta, \tau)$ )
18:  return  $\Delta_{tx}$ 
19: end procedure

20: procedure RFDECODER( $\Delta_{tx}, \Psi_{rf}$ )
21:   $\mathbf{B}_{rec} \leftarrow$  empty list
22:   $(\Delta, \tau) \leftarrow$  GetData( $\Delta_{tx}$ )
23:  WaitForTransmission( $\tau$ )
24:   $\mathbf{B}_{\Delta} \leftarrow$  DecDelta( $\Delta$ )
25:  for each  $(\pi, F_{\Delta}) \in \mathbf{B}_{\Delta}$  do
26:     $F_{rf} \leftarrow$  RenderViewFromRF( $\Psi_{rf}, \pi$ )
27:     $F_{rec} \leftarrow$  RecCAVFrame( $F_{rf}, F_{\Delta}$ )
28:    Add( $\mathbf{B}_{rec}, F_{rec}$ )
29:  end for
30:  return  $\mathbf{B}_{rec}$ 
31: end procedure

```

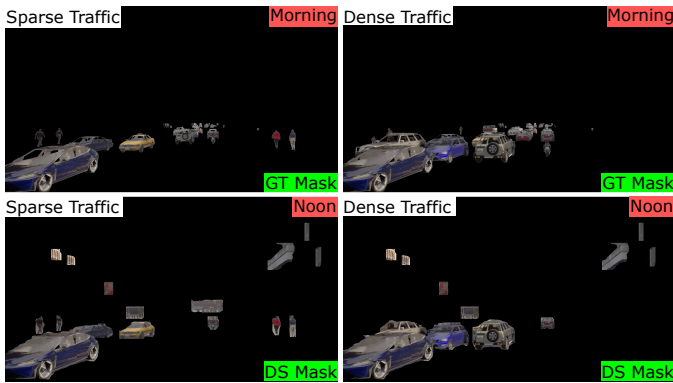


Fig. 4. Delta-frames extracted using GT Masks from the simulator and using proposed DS algorithm in both sparse and dense traffic in noon conditions.

may not be accurately recognized due to the limitations in the simulator’s photorealism. A limitation of this approach is the incorrect segmentation of objects or irrelevant differences, which can be mitigated by considering object location and

shape consistency across multiple frames, to discard such visual artifacts.

V. EXPERIMENTAL RESULTS

An experimental setup was established in a virtual urban environment using the CARLA simulator to validate this approach. This setup aimed to replicate real-world urban scenarios within a controlled, simulated environment, providing a robust platform for testing the efficacy of the RF-based compression system in an urban CAV context.

The simulation results of the RFDVC approach are obtained using simulation code that we have made available in an online GitHub repository¹.

A. Simulation Parameters

To ensure reproducibility, we provide key details on the simulation environment, dataset used, and model configurations. Table II outlines the parameters used in the CARLA simulator. Specifically, we used CARLA version 9.15 with the Town10 map. Nine cameras were employed during training, while three were used during deployment, with all cameras capturing images at a resolution of 1920x1080 pixels. The motion blur intensity was set to zero, the focal distance was 1000 unreal engine (UE) units, and the field of view (FOV) was 90°.

TABLE II
PARAMETERS OF CARLA SIMULATOR.

Parameter	Value
CARLA version	9.15
Map	Town10
Cameras during training / deployment	9 / 3
Resolution of cameras & images	1920x1080
Motion blur intensity	0
Focal distance	1000 UE units
FOV	90°

Table III details the datasets utilized for training and deployment under morning conditions. The training dataset was collected in an empty environment, with no traffic, pedestrians, or vehicles, resulting in 9 213 images. For deployment, two scenarios were considered: sparse traffic with 60 pedestrians and 100 vehicles, yielding 17 956 images, and dense traffic with 60 pedestrians and 200 vehicles, producing 11 992 images. Fig. 5 illustrates the diverse conditions and traffic density as generated by the CARLA simulator. The morning conditions scenario is employed for training the RF models 3DGS and INGP. Conditions at noon, evening, and during wet conditions are closely aligned with the morning scenario, making the generation of delta-frames relatively straightforward. In contrast, fog and rain conditions differ significantly from the morning conditions, presenting greater challenges in the production of delta-frames. Additionally, the more adverse conditions make it difficult to identify dissimilarities in the images, which necessitates omitting these conditions from our DS experiments.

¹<https://github.com/Maftej/rfdvc>

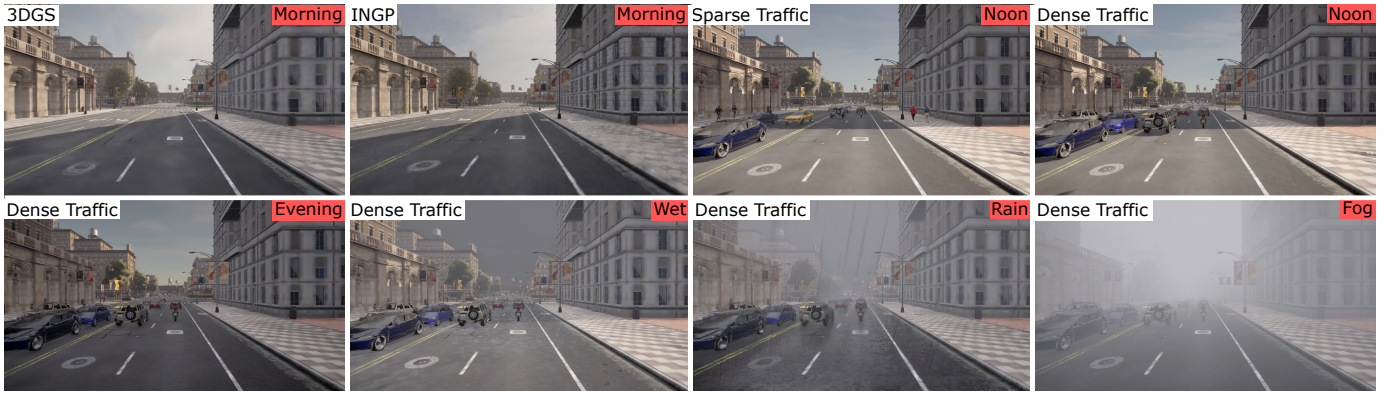


Fig. 5. CAV-frames from both sparse and dense traffic in noon, evening, wet, rain and fog conditions. RF-frames trained in morning conditions.

TABLE III
DATASET FOR TRAINING AND DEPLOYMENT.

Dataset	Traffic	Pedestrians	Vehicles	Images
Training	Empty	0	0	9 213
Deployment	Sparse	60	100	17 956
Deployment	Dense	60	200	11 992

We employed RF models INGP and 3DGS using the nerf-studio library, configured with the FOV and image resolution specified in Table II. Both models were trained for 30 000 iterations.

B. Quantitative Evaluation of RF Models

To assess potential quality degradation introduced by RFs and the impact of environmental changes, we employed key image quality metrics: peak signal-to-noise ratio (PSNR), SSIM, and learned perceptual image patch similarity (LPIPS). These metrics evaluate differences in pixel values, structural features, and perceptual quality, respectively.

TABLE IV
QUANTITATIVE EVALUATION OF INGP AND 3DGS MODELS.

Area	INGP			3DGS		
	PSNR \uparrow	SSIM \uparrow	LPIPS \downarrow	PSNR \uparrow	SSIM \uparrow	LPIPS \downarrow
a_1	20.68	0.65	0.53	25.17	0.78	0.41
a_2	19.99	0.58	0.52	25.37	0.78	0.41
a_3	21.25	0.63	0.49	28.35	0.84	0.34
a_4	19.38	0.56	0.53	25.20	0.77	0.41
a_5	21.10	0.64	0.47	28.94	0.86	0.32
a_6	20.81	0.58	0.53	27.03	0.81	0.36
a_7	20.52	0.58	0.52	27.15	0.82	0.35
a_8	20.87	0.50	0.61	26.62	0.72	0.45
a_9	20.34	0.60	0.53	25.70	0.78	0.41
a_{10}	19.85	0.55	0.55	25.77	0.81	0.38
a_{11}	21.91	0.65	0.51	27.98	0.82	0.37
a_{12}	21.38	0.67	0.48	26.14	0.82	0.38
a_{13}	19.41	0.58	0.51	25.54	0.80	0.39
a_{14}	18.99	0.54	0.52	23.58	0.73	0.44
a_{15}	20.12	0.51	0.50	24.81	0.71	0.39
a_{16}	19.36	0.56	0.56	25.01	0.78	0.46
a_{17}	20.71	0.65	0.48	26.13	0.80	0.37
a_{18}	22.44	0.69	0.47	27.20	0.82	0.37
a_{19}	19.99	0.52	0.51	28.18	0.84	0.34

Table IV presents the average PSNR, SSIM, and LPIPS values for both INGP and 3DGS models across various areas.

In the INGP models, area a_{18} achieved the highest PSNR of 22.44, indicating better image fidelity, while area a_{14} recorded the lowest PSNR of 18.99, suggesting degradation. SSIM values were highest in area a_{12} and lowest in area a_{10} . For LPIPS, area a_5 performed best, whereas area a_8 exhibited the highest perceptual dissimilarity.

In comparison, the 3DGS models generally showed higher PSNR and SSIM values, with area a_5 excelling in both PSNR 28.94 and LPIPS 0.32. However, area a_{14} underperformed, demonstrating the lowest PSNR and higher LPIPS, indicating potential issues in perceptual quality.

C. Data Savings in Different Conditions

A primary feature of RFDVC is its substantial data savings compared to the commonly used and highly efficient H.264 and H.265 codecs. For URLLC, frames are transmitted in batches of up to 10 at 30 FPS to support real-time communication. Images are encoded with consistent configurations across both H.264 and RFDVC, with the latter leveraging adaptive quantization to more effectively compress black regions containing no information relevant to downstream tasks. Furthermore, we evaluate delta-frame encoding using GT masks as an upper bound for compression efficiency against our DS algorithm, which offers a realistic encoding approach to capture most differences without restrictions to class categories, as in methods such as YOLO or other DL models used in computer vision tasks.

Fig. 6 displays a box plot comparing the data savings achieved by RFDVC and VC when using either the DS algorithm or GT masks for transmitting data from camera sensors under noon, evening, and wet conditions. While static RF models are applied, the conditions within these models do not align precisely with actual conditions, resulting in lighting discrepancies, particularly under wet scenarios. For RFDVC with the DS algorithm, the interquartile range of data savings spans 55% to 75% with the H.264 codec and 30% to 45% with the H.265 codec. Higher resolutions provide greater data savings as larger black regions are more effectively encoded. With GT masks, data savings vary from approximately 65%

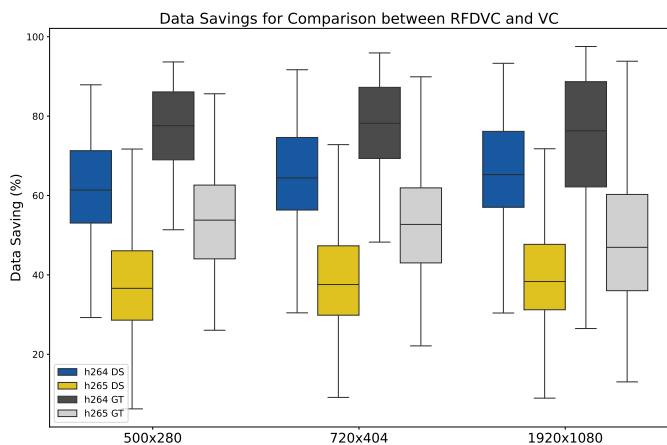


Fig. 6. RFDVC data savings using DS method and GT masks in noon, evening and wet conditions.

to 90% using the H.264 codec and from 40% to 60% using the H.265 codec.

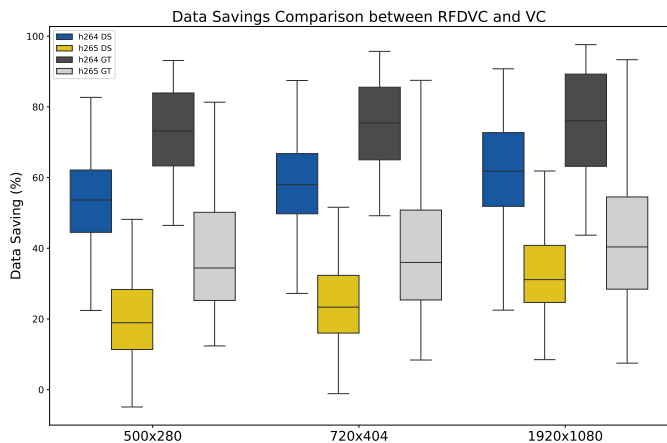


Fig. 7. RFDVC data savings using DS method and GT masks in rain conditions.

Fig. 7 illustrates the data savings achieved by RFDVC compared to VC under rain conditions, which pose a more challenging environment due to substantial lighting changes and partial frame corruption from heavy rainfall. Despite these challenging conditions, data savings fall within an interquartile range of 45% to 70% with the H.264 codec and 15% to 40% with the H.265 codec. Using GT masks, data savings are approximately 63% to 90% with the H.264 codec and 25% to 50% with the H.265 codec.

Fig. 8 depicts the data savings achieved by RFDVC in comparison to VC under fog conditions with H.264 and H.265 codecs. Fog presents particular challenges due to limited visibility, partial object discernibility, and an increase in low-frequency signals resulting from fog's uniformity. This uniformity eases encoding but complicates object segmentation for the DS algorithm due to the partial visibility of objects. Data savings within the interquartile range are between 25% and 60% with the H.264 codec, whereas savings range from -50%

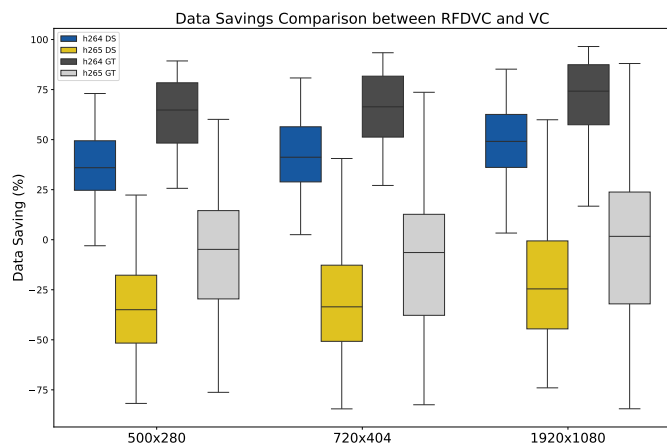


Fig. 8. RFDVC data savings using DS method and GT masks in fog conditions.

to 0% with the H.265 codec. Using GT masks, data savings fall within an interquartile range of approximately 50% to 80% with the H.264 codec and from -30% to 20% with the H.265 codec.

D. Packet Loss

We simulate packet loss using the Gilbert-Elliott model to demonstrate that the RFDVC approach surpasses standard H.264 and H.265 codecs, even under packet loss conditions. The RFDVC method shows greater effectiveness in ensuring that all critical information is reliably transmitted across the network, a crucial requirement for real-time and sensitive communication. This advantage is especially significant in the context of CAVs, where safety and reliability must be maintained across diverse operational scenarios.

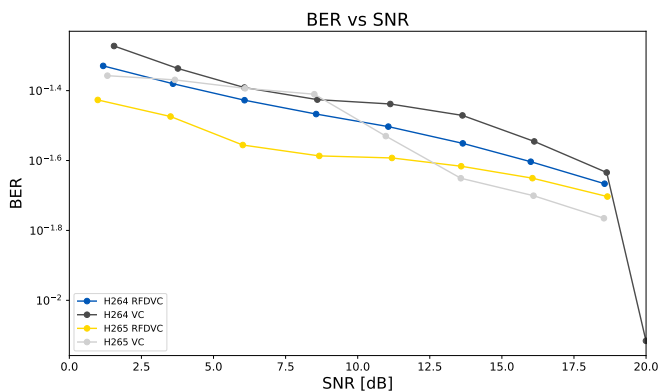


Fig. 9. Packet loss simulation using RFDVC and VC approaches with data encoded using H.264 and H.265 codecs.

Fig. 9 presents the comparison of bit error rate (BER) versus signal-to-noise ratio (SNR) between the proposed RFDVC approach and the conventional H.264 and H.265 codecs. The RFDVC method exhibits greater stability over a wide range of SNR values, achieving a lower BER of approximately $10^{-1.6}$ at an SNR of 10dB, compared to the $10^{-1.4}$ observed

with standard H.264 coding. This consistent BER reduction across increasing SNR levels highlights RFDVC's enhanced resilience to noise and packet loss, supporting more reliable data transmission. These findings confirm that our approach improves performance by maintaining communication quality, even under challenging network conditions.

VI. CONCLUSION

In this work, we propose RFDVC approach, based on RF-encoder and RF-decoder architecture, for V2I communication and P2V synchronization within the vehicular metaverse. Distributed RFs serve as DTs storing photorealistic 3D scene in compressed form. An experimental setup was established in a virtual urban environment using the CARLA simulator divided into 19 areas represented as RFs. The experimental results show that RFDVC achieves significant data savings up to 90% against H.264 codec and 45% against H.265 codec in variety of conditions including lighting changes, rain and fog. RFDVC exhibits greater resilience to transmission errors, achieving a BER of approximately $10^{-1.6}$ at SNR of 10 dB, compared to $10^{-1.4}$ for standard VC.

Future research will prioritize the processing of downstream tasks in advance within the vehicular metaverse, alongside adaptive updates to RFs as required. This strategy aims to minimize latency and improve virtual environment accuracy, thereby optimizing real-time performance for sophisticated vehicular applications in complex and data-rich scenarios.

ACKNOWLEDGMENT

This work was supported by the Ministry of Education, Science, Research and Sport of the Slovak Republic, and the Slovak Academy of Sciences under Grant VEGA 1/0685/23 and by the Slovak Research and Development Agency under Grant APVV SK-CZ-RD-21-0028 and APVV-23-0512, and by Research and Innovation Authority VAIA under Grant 09I03-03-V04-00395. We would also like to acknowledge that Figs. 2 and 3 were made using licensed vector graphics available at Freepik.com

REFERENCES

- [1] L. Chen, S. Teng, B. Li, X. Na, Y. Li, Z. Li, J. Wang, D. Cao, N. Zheng, and F.-Y. Wang, "Milestones in autonomous driving and intelligent vehicles—part ii: Perception and planning," *IEEE Transactions on Systems, Man, and Cybernetics: Systems*, vol. 53, no. 10, pp. 6401–6415, 2023.
- [2] A. Islam, A. Debnath, M. Ghose, and S. Chakraborty, "A survey on task offloading in multi-access edge computing," *Journal of Systems Architecture*, vol. 118, p. 102225, 2021. [Online]. Available: <https://www.sciencedirect.com/science/article/pii/S1383762121001570>
- [3] L. U. Khan, M. Guizani, D. Niyato, A. Al-Fuqaha, and M. Debbah, "Metaverse for wireless systems: Architecture, advances, standardization, and open challenges," *Internet of Things*, vol. 25, p. 101121, 2024. [Online]. Available: <https://www.sciencedirect.com/science/article/pii/S2542660524000635>
- [4] M. Xu, D. Niyato, B. Wright, H. Zhang, J. Kang, Z. Xiong, S. Mao, and Z. Han, "Epvisa: Efficient auction design for real-time physical-virtual synchronization in the human-centric metaverse," *IEEE Journal on Selected Areas in Communications*, vol. 42, no. 3, pp. 694–709, 2024.
- [5] Y. Qiu, M. Chen, H. Huang, W. Liang, J. Liang, Y. Hao, and D. Niyato, "Spotlighter: Backup age-guaranteed immersive virtual vehicle service provisioning in edge-enabled vehicular metaverse," *IEEE Transactions on Mobile Computing*, pp. 1–17, 2024.
- [6] H. Alves, G. D. Jo, J. Shin, C. Yeh, N. H. Mahmood, C. H. M. de Lima, C. Yoon, G. Park, N. Rahatheva, O.-S. Park, and et al., "Beyond 5G urllc evolution: New service modes and practical considerations," *ITU Journal on Future and Evolving Technologies*, vol. 3, no. 3, p. 545–554, 2022.
- [7] D. Ding, Z. Ma, D. Chen, Q. Chen, Z. Liu, and F. Zhu, "Advances in video compression system using deep neural network: A review and case studies," *Proceedings of the IEEE*, vol. 109, no. 9, pp. 1494–1520, 2021.
- [8] R. Birman, Y. Segal, and O. Hadar, "Overview of research in the field of video compression using deep neural networks," *Multimedia Tools and Applications*, vol. 79, pp. 11 699–11 722, 2020.
- [9] Y. Zhang, T. van Rozendaal, J. Brehmer, M. Nagel, and T. Cohen, "Implicit neural video compression," *arXiv preprint arXiv:2112.11312*, 2021.
- [10] H. Chen, B. He, H. Wang, Y. Ren, S. N. Lim, and A. Shrivastava, "Nerv: Neural representations for videos," in *Advances in Neural Information Processing Systems*, M. Ranzato, A. Beygelzimer, Y. Dauphin, P. Liang, and J. W. Vaughan, Eds., vol. 34. Curran Associates, Inc., 2021, pp. 21 557–21 568. [Online]. Available: https://proceedings.neurips.cc/paper_files/paper/2021/file/b44182379bf9fae976e6ae5996e13cd8-Paper.pdf
- [11] A. Ghorbel, W. Hamidouche, and L. Morin, "Nerv++: An enhanced implicit neural video representation," 2024. [Online]. Available: <https://arxiv.org/abs/2402.18305>
- [12] Z. Chen, G. Lu, Z. Hu, S. Liu, W. Jiang, and D. Xu, "LSVC: A learning-based stereo video compression framework," in *Proceedings of the IEEE/CVF Conference on Computer Vision and Pattern Recognition*, 2022, pp. 6073–6082.
- [13] Y. Wu, K. Zhang, and Y. Zhang, "Digital twin networks: A survey," *IEEE Internet of Things Journal*, vol. 8, no. 18, pp. 13 789–13 804, 2021.
- [14] O. Hashash, C. Chaccour, W. Saad, K. Sakaguchi, and T. Yu, "Towards a decentralized metaverse: Synchronized orchestration of digital twins and sub-metaverses," 2022. [Online]. Available: <https://arxiv.org/abs/2211.14686>
- [15] L. U. Khan, W. Saad, D. Niyato, Z. Han, and C. S. Hong, "Digital-twin-enabled 6g: Vision, architectural trends, and future directions," *IEEE Communications Magazine*, vol. 60, no. 1, pp. 74–80, 2022.
- [16] S. Mihai, M. Yaqoob, D. V. Hung, W. Davis, P. Towakel, M. Raza, M. Karamanoglu, B. Barn, D. Shetve, R. V. Prasad, H. Venkataraman, R. Trestian, and H. X. Nguyen, "Digital Twins: A Survey on Enabling Technologies, Challenges, Trends and Future Prospects," *IEEE Communications Surveys and Tutorials*, vol. 24, no. 4, pp. 2255–2291, 2022.
- [17] M. Xu, W. C. Ng, W. Y. B. Lim, J. Kang, Z. Xiong, D. Niyato, Q. Yang, X. Shen, and C. Miao, "A Full Dive Into Realizing the Edge-Enabled Metaverse: Visions, Enabling Technologies, and Challenges," *IEEE Communications Surveys and Tutorials*, vol. 25, no. 1, pp. 656–700, 2023.
- [18] Y. Ren, R. Xie, F. R. Yu, T. Huang, and Y. Liu, "Quantum Collective Learning and Many-to-Many Matching Game in the Metaverse for Connected and Autonomous Vehicles," *IEEE Transactions on Vehicular Technology*, vol. 71, no. 11, pp. 12 128–12 139, 2022.
- [19] M. Xu, D. Niyato, H. Zhang, J. Kang, Z. Xiong, S. Mao, and Z. Han, "Generative AI-empowered Effective Physical-Virtual Synchronization in the Vehicular Metaverse," 2023.
- [20] P. Zhou, J. Zhu, Y. Wang, Y. Lu, Z. Wei, H. Shi, Y. Ding, Y. Gao, Q. Huang, Y. Shi, A. Alhilal, L.-H. Lee, T. Braud, P. Hui, and L. Wang, "Vetaverse: A Survey on the Intersection of Metaverse, Vehicles, and Transportation Systems," 2023.
- [21] B. Mildenhall, P. P. Srinivasan, M. Tancik, J. T. Barron, R. Ramamoorthi, and R. Ng, "Nerf: Representing scenes as neural radiance fields for view synthesis," in *Computer Vision – ECCV 2020*, A. Vedaldi, H. Bischof, T. Brox, and J.-M. Frahm, Eds. Cham: Springer International Publishing, 2020, pp. 405–421.
- [22] J. T. Barron, B. Mildenhall, M. Tancik, P. Hedman, R. Martin-Brualla, and P. P. Srinivasan, "Mip-nerf: A multiscale representation for anti-aliasing neural radiance fields," in *2021 IEEE/CVF International Conference on Computer Vision (ICCV)*, 2021, pp. 5835–5844.
- [23] J. T. Barron, B. Mildenhall, D. Verbin, P. P. Srinivasan, and P. Hedman, "Zip-nerf: Anti-aliased grid-based neural radiance fields," in *2023 IEEE/CVF International Conference on Computer Vision (ICCV)*, 2023, pp. 19 640–19 648.
- [24] T. Müller, A. Evans, C. Schied, and A. Keller, "Instant neural graphics primitives with a multiresolution hash encoding," *ACM Transactions on Graphics (ToG)*, vol. 41, no. 4, pp. 1–15, 2022.

- [25] B. Kerbl, G. Kopanas, T. Leimkühler, and G. Drettakis, “3D Gaussian Splatting for Real-Time Radiance Field Rendering,” 2023.
- [26] L. He, L. Li, W. Sun, Z. Han, Y. Liu, S. Zheng, J. Wang, and K. Li, “Neural radiance field in autonomous driving: A survey,” 2024. [Online]. Available: <https://arxiv.org/abs/2404.13816>
- [27] M. Tancik, V. Casser, X. Yan, S. Pradhan, B. P. Mildenhall, P. Srinivasan, J. T. Barron, and H. Kretzschmar, “Block-nerf: Scalable large scene neural view synthesis,” in *2022 IEEE/CVF Conference on Computer Vision and Pattern Recognition (CVPR)*, 2022, pp. 8238–8248.
- [28] D. Duckworth, P. Hedman, C. Reiser, P. Zhizhin, J.-F. Thibert, M. Lučić, R. Szeliski, and J. T. Barron, “Smerf: Streamable memory efficient radiance fields for real-time large-scene exploration,” *ACM Trans. Graph.*, vol. 43, no. 4, jul 2024. [Online]. Available: <https://doi.org/10.1145/3658193>
- [29] R. Li, S. Fidler, A. Kanazawa, and F. Williams, “Nerf-xl: Scaling nerfs with multiple gpus,” 2024.
- [30] B. Kerbl, A. Meuleman, G. Kopanas, M. Wimmer, A. Lanvin, and G. Drettakis, “A hierarchical 3d gaussian representation for real-time rendering of very large datasets,” *ACM Transactions on Graphics*, vol. 43, no. 4, July 2024. [Online]. Available: <https://repo-sam.inria.fr/fungraph/hierarchical-3d-gaussians/>
- [31] A. Pun, G. Sun, J. Wang, Y. Chen, Z. Yang, S. Manivasagam, W.-C. Ma, and R. Urtasun, “Neural lighting simulation for urban scenes,” in *Advances in Neural Information Processing Systems*, A. Oh, T. Naumann, A. Globerson, K. Saenko, M. Hardt, and S. Levine, Eds., vol. 36. Curran Associates, Inc., 2023, pp. 19 291–19 326. [Online]. Available: https://proceedings.neurips.cc/paper_files/paper/2023/file/3d7259031023c5aa463187c4a31c95c8-Paper-Conference.pdf
- [32] X. Zhou, Z. Lin, X. Shan, Y. Wang, D. Sun, and M.-H. Yang, “Drivinggaussian: Composite gaussian splatting for surrounding dynamic autonomous driving scenes,” in *Proceedings of the IEEE/CVF Conference on Computer Vision and Pattern Recognition (CVPR)*, June 2024, pp. 21 634–21 643.
- [33] Z. Wu, T. Liu, L. Luo, Z. Zhong, J. Chen, H. Xiao, C. Hou, H. Lou, Y. Chen, R. Yang *et al.*, “Mars: An instance-aware, modular and realistic simulator for autonomous driving,” *arXiv preprint arXiv:2307.15058*, 2023.
- [34] Y. Liu, X. Tu, D. Chen, K. Han, O. Altintas, H. Wang, and J. Xie, “Visualization of Mobility Digital Twin: Framework Design, Case Study, and Future Challenges,” in *2023 IEEE 20th International Conference on Mobile Ad Hoc and Smart Systems (MASS)*. IEEE, 2023, pp. 170–177.
- [35] E. Ślapak, M. Dopiriak, M. A. Al Faruque, J. Gazda, and M. Levorato, “Distributed radiance fields for edge video compression and metaverse integration in autonomous driving,” in *2024 IEEE International Conference on Smart Computing (SMARTCOMP)*, 2024, pp. 71–76.
- [36] A. Kirillov, E. Mintun, N. Ravi, H. Mao, C. Rolland, L. Gustafson, T. Xiao, S. Whitehead, A. C. Berg, W.-Y. Lo, P. Dollar, and R. Girshick, “Segment anything,” in *Proceedings of the IEEE/CVF International Conference on Computer Vision (ICCV)*, October 2023, pp. 4015–4026.
- [37] X. Zhao, W. Ding, Y. An, Y. Du, T. Yu, M. Li, M. Tang, and J. Wang, “Fast segment anything,” 2023. [Online]. Available: <https://arxiv.org/abs/2306.12156>